

Cite this: DOI: 10.1039/xxxxxxxxxx

Inflow boundary conditions determine T-mixer efficiency†

Tobias Schikarski,^a Holger Trzenschiok,^a Wolfgang Peukert,^a and Marc Avila^b

Received Date
Accepted Date

DOI: 10.1039/xxxxxxxxxx

www.rsc.org/journalname

We report on a comprehensive experimental-computational study of a simple T-shaped mixer for Reynolds numbers up to 4000. In the experiments, we determine the mixing time by applying the Villiermaux–Dushman characterization to a water–water mixture. In the numerical simulations, we resolve down to the smallest (Kolmogorov) flow scales in space and time. Excellent agreement is obtained between the experimentally measured mixing time and numerically computed intensity of segregation, especially in the turbulent regime, which validates both approaches. We confirm that the mixing time is mainly determined by the specific power input, as assumed in most mixing-models. However, we show that by suitably manipulating the inflow conditions, the power input necessary to achieve a given mixing time can be reduced by a factor of six. Our study enables detailed investigations of the influence of hydrodynamics on chemical reactions and precipitation processes, as well as the detailed testing of turbulence and micromixing models.

1 Introduction

The quality of mixing determines the efficiency of many chemical reactions in fluids. Examples are chemical synthesis^{1–3} and particle synthesis, such as fast precipitation of inorganic⁴ and organic compounds^{5,6}. At the interface of two mixing fluids, mass is exchanged between both fluids by diffusion, a process usually referred to as *micromixing*^{7,8}. The rate of mass transfer is quantified by the diffusion flux, which is the product of the area of the fluid interface and the diffusion coefficient D . As the diffusion coefficient is very small in liquid mixtures ($D \sim 10^{-9} \text{ m}^2/\text{s}$), the key in accelerating mixing is the enlargement of the fluid interface via vortices in turbulent flow, termed *macromixing*. Hence sophisticated designs have been proposed to enhance turbulence and thereby optimize mixing⁹. However, the commonly accepted view is that the specific power input is the only effective parameter, i.e. improvements in mixing efficiency due to geometrical optimizations are associated with increased energy dissipation¹⁰. In this paper, we provide direct experimental and numerical evidence that manipulation of the inflow conditions can significantly improve the mixing performance without increasing the energy consumption.

We consider a water–water mixture in the T-mixer shown in Fig. 1(a) because of its simplicity, which allows a better under-

standing of the underlying physicochemical mechanisms. The main control parameter is the power input, which depends on the Reynolds number $Re = u_0 d / \nu$, where d is the hydraulic diameter of the inlet, u_0 the mean inlet velocity and ν is the kinematic viscosity of the fluid. The Schmidt number $Sc = \nu / D$ sets the ratio of mass to momentum diffusion and is also an important parameter in mixing (in liquids, $Sc = \mathcal{O}(10^3)$). Steady and unsteady low Re regimes have been intensively investigated in recent years by means of simulation and experiments with good agreement^{11–19}. Nevertheless, the turbulent mixing at $Re > 2000$ has not been investigated so far, neither in experiments nor in simulations. This is surprising in view that in most applications the flow is well into the turbulent regime.

In what follows, we present a detailed analysis of the mixing regimes encountered in the T-mixer as Re increases up to 4000, see Fig. 1(b)–(h). We solve the Navier–Stokes equations using direct numerical simulation (DNS), whereby all scales of fluid motion are resolved in space and time²⁰. This method stands out because it is free of empirical parameters, which in more commonly applied approaches such as RANS or plug-flow reactor models are needed to model turbulence. However, DNS remains mainly a research tool because of its high computing cost. For example, our DNS at $Re = 4000$ required 1.4 million cores hours at the cluster MEGGIE of the Erlangen Regional Computing Center (RRZE) in order to obtain converged statistics.

In our experiments, we use the competitive-parallel Villiermaux–Dushman reaction to determine the mixing time²¹. By adapting the concentration of the chemicals and transforming the measured quantities to concentration-independent mixing times, we characterize mixing from the laminar to the fully turbulent regime $100 \leq Re \leq 4000$.

^a Institute of Particle Technology, Department of Chemical and Biological Engineering, Friedrich-Alexander-Universität Erlangen-Nürnberg, 91058 Erlangen, Germany; E-mail: tobias.schikarski@fau.de

^b Center of Applied Space Technology and Microgravity, Universität Bremen, Am Fallturm, 28359 Bremen, Germany

† Electronic Supplementary Information (ESI) available: [details of any supplementary information available should be included here]. See DOI: 10.1039/b000000x/

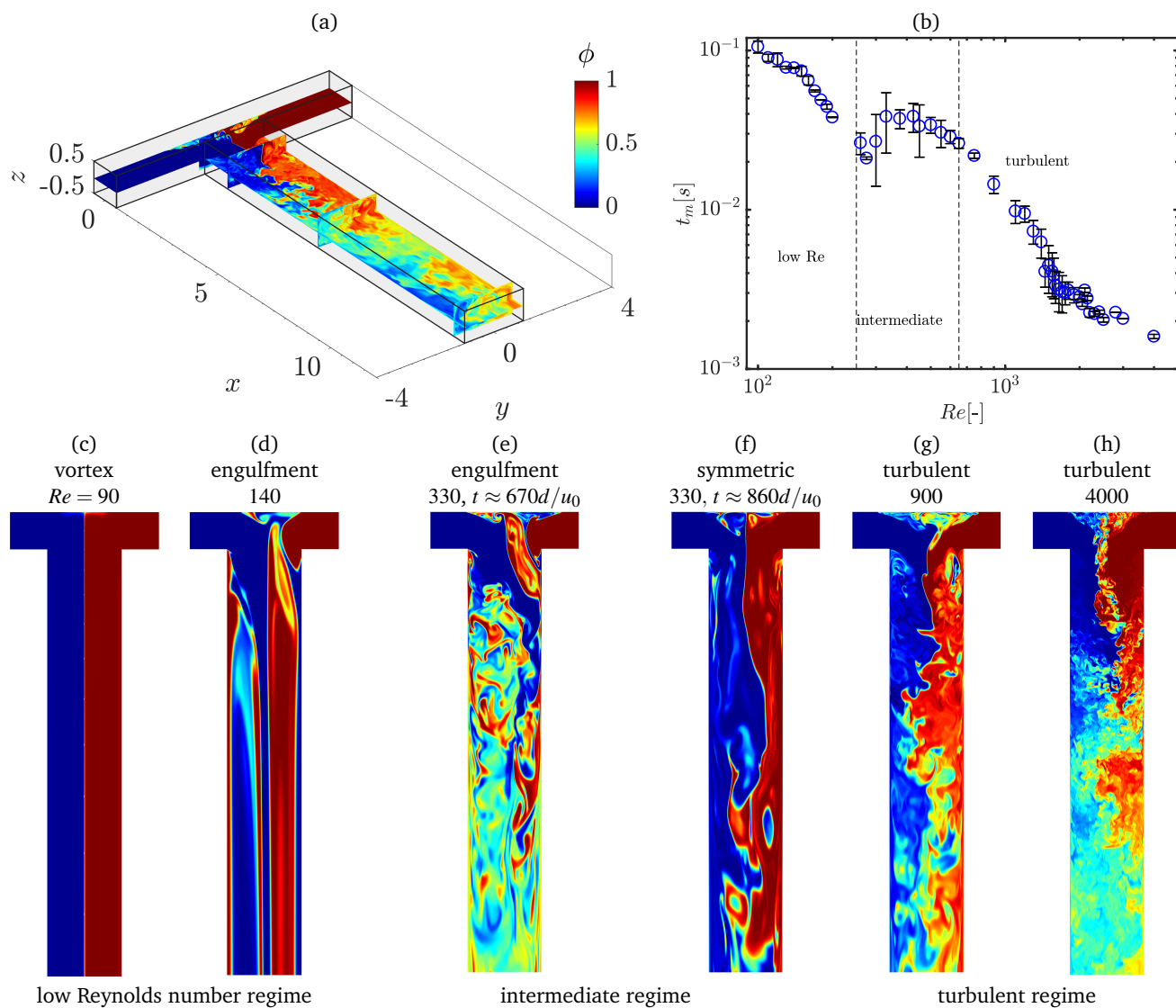


Fig. 1 (Color online) (a) T-mixer showing an instantaneous snapshot of passive scalar ϕ at $Re = 200$, illustrated by four (y, z) -cross sections and one (x, y) -cross section which hereafter are used to visualize the flow and passive scalar behavior. (b) Experimentally measured mixing time t_m as function of Reynolds number Re . Error bars indicate the standard deviation of t_m which is extracted from a sample of at least three measurements. (c)–(h) Instantaneous snapshots of passive scalar ϕ at cross section $z = -0.25$ illustrating the mixing regimes considered within this work.

2 Methods

Our T-mixer consists of two inlets of square crosssection with hydraulic diameter $d = 1\text{mm}$, which discharge in a mixing channel of 1mm height, 2mm width and 11.5mm length. This results in identical mean velocity (u_0) for the inlets and the mixing channel. In the experiment, the inlets are 18mm long to allow the flow profiles to develop before entering the mixing channel. Note however, that the dimensionless length to achieve a fully developed laminar flow profile is $L/d = 0.05Re$. Hence, in our experiments fully developed laminar flow could only be achieved up to $Re = 360$. By contrast, fully developed turbulent profiles require $L/d = 4.4Re^{1/6}$ only^{22,23}, which was always satisfied in our experiments. In the numerical simulations, fully developed flows were imposed at the inlet boundary. This allowed using inlets of just 3mm in length, drastically reducing the computational effort.

2.1 Numerical model

We use Cartesian coordinates x^* , y^* , z^* with the origin located in the center of the junction, y^* defined along the opposing inlet channels and x^* defined along the streamwise direction of the outlet channel. Lengths are made dimensionless by scaling with the hydraulic diameter, $x = x^*/d$, $y = y^*/d$, $z = z^*/d$, whereas velocities are made dimensionless with u_0 . The mixing process is governed by the dimensionless incompressible Navier–Stokes equations

$$\frac{\partial \vec{u}}{\partial t} + \vec{u} \cdot \nabla \vec{u} = -\nabla p + \frac{1}{Re} \Delta \vec{u}, \quad \nabla \cdot \vec{u} = 0, \quad (1)$$

coupled a the convection-diffusion equation for the concentration

$$\frac{\partial \phi}{\partial t} + \vec{u} \cdot \nabla \phi = \frac{1}{ReSc} \Delta \phi, \quad (2)$$

where p is the pressure, $\phi \in [0,1]$ is a passive scalar and $\vec{u} = (u, v, w)$ is the velocity field.

2.1.1 Spatial and temporal resolution of mixing processes

We discretized eq. (1) with the finite-volume method in space and an explicit low storage Runge–Kutta scheme in time, both of 2^{nd} order, by using the high-performance-code FASTEST3D¹⁸. Because our simulations solved for all fluid (eddy) motions in space and time, macromixing was simulated with very high fidelity. To ensure this, the criterion $h \lesssim 2\eta$ was applied, where $h = \max(\Delta x, \Delta y, \Delta z)$ is the local grid spacing and η is the smallest (Kolmogorov) flow scale. It is defined as $\eta = (v^3/\epsilon)^{1/4}$, where ϵ is the dissipation of the turbulent kinetic energy. This resulted in almost 200 million grid points for the highest Reynolds number considered ($Re = 4000$). Furthermore, to enforce the stability of our explicit Runge-Kutta scheme, a constant time step was chosen such that the CFL number $c = |u/\Delta x| + |v/\Delta y| + |w/\Delta z| < 0.3$.

The smallest length scale of the scalar field is termed Batchelor scale (η_b) and is related to the Kolmogorov scale via the Schmidt number, $\eta_b = \eta/\sqrt{Sc}$. In the range of scales between the Kolmogorov and the Batchelor scales, micromixing takes place. Here the velocity field features no fluctuations, whereas the scalar field fluctuates. Although micromixing has been sometimes argued to be the rate-limiting step in liquid mixing²⁴, it cannot be resolved

in the simulations because of $Sc = \mathcal{O}(10^3)$. In practice, spatial discretization schemes and subgrid modeling introduce a further diffusion term in Eq. 2, with a corresponding artificial diffusion coefficient. This artificial diffusion coefficient depends on the local grid size, numerical scheme and subgrid model, and is in general larger than the natural diffusion coefficient.

In our simulations, the Schmidt number is $Sc = 600$, so resolving the Batchelor scale would require over 6×10^{12} grid points at $Re = 4000$. As this is computationally infeasible, we treat the convective term in Eq. 2 to ensure a bounded value of ϕ and a nearly 2^{nd} order approximation despite the high Peclet numbers $Pe = ReSc$. This is accomplished by using linear schemes with flux limiters fulfilling the total variation diminishing criteria²⁵. In a nutshell, our scheme essentially adds diffusion (locally in space and time), when large gradients of ϕ appear. A complete description of the numerical technique used herein and a thorough validation is given in Schikarski *et al.*¹⁸.

2.1.2 Boundary conditions: flow regimes in a square duct

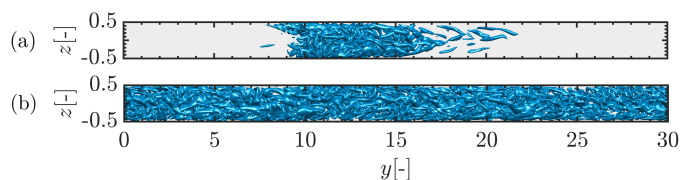


Fig. 2 Turbulent flow in a square duct driven by a constant volume flux. The boundary conditions are periodic in the streamwise direction in a domain of length $30d$. (a) Localized turbulent puff at $Re = 1700$. (b) Fully turbulent flow at $Re = 2500$. Instantaneous isosurfaces of normalized Q -criteria with threshold $Q = 1$ ²⁶.

Because of the wide range of $90 \leq Re \leq 4000$ covered in our simulations, special care must be taken with the inlet boundary conditions. At low Re , the flow in a square duct is always laminar. In fact, laminar square-duct flow is linearly stable at all Re and in DNS it is necessary to disturb the flow in order to generate turbulence via nonlinearities. In the presence of strong disturbances, localized turbulent puffs were observed in experiments²⁷ and numerical simulations²⁸ for $Re \gtrsim 1430$, see Fig. 2(a). In fact, Osborne Reynolds had already observed such puffs in his classical experiments of cylindrical pipe flow²⁹. As Re increases, puffs occur with increased probability^{30,31}, until the puff regime is replaced by fully turbulent flow at $Re \gtrsim 2030$ ³². A snapshot of fully turbulent flow at $Re = 2500$ is shown in Fig. 2(b).

A full understanding of the dynamics of transition in pipes and ducts has just emerged in the last decade. The interested reader is referred to Barkley³³ for a recent comprehensive review. Here, we briefly summarize the main point for engineering purposes. For $Re \gtrsim 1430$ the flow in a square duct can either be laminar or turbulent depending on the level of disturbance. For example, Osborne Reynolds could keep the flow laminar up to $Re \approx 12,000$ with a purposely designed entrance and with the fluid settled in the supply tank²⁹. However, in conventional setups used in chemical engineering like ours, the occurrence of turbulent puffs, separated by segments of laminar flow, is a random process con-

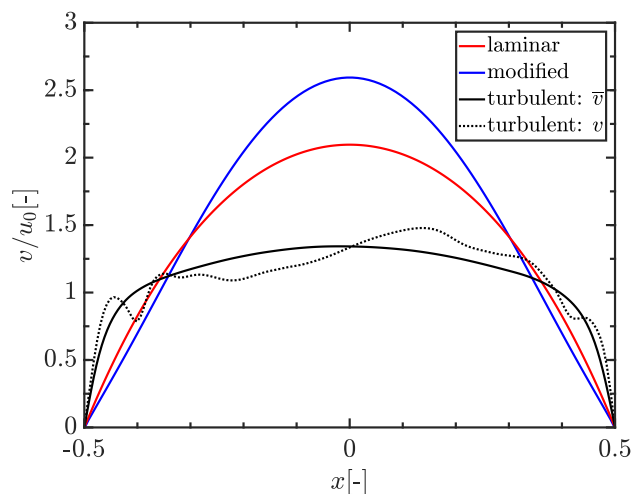


Fig. 3 Inlet velocity profiles v at mid-height ($z = 0$) used as boundary condition for the left inflow channel ($y < 0$). The laminar and modified laminar inflow velocities are steady, whereas for turbulent inflow the boundary conditions are time-dependent. An instantaneous profile v and the time-averaged profile \bar{v} at $Re = 4000$ are shown here for clarity.

trolled by imperfections and natural disturbances. This *natural* onset of turbulence occurred in our experiments at $Re \approx 1400$, as shown in Fig. S1 of the ESI†. Finally, it is worth noting that at a given Reynolds number, the flow in the T-mixer is much more turbulent than in a square-duct. For example, the level of turbulence reached near the junction at $Re = 4000$ is similar to that of cylindrical pipe flow at $Re \approx 6 \times 10^4$ (see S2 in ESI†).

In our numerical simulations, we tested the influence of the inflow conditions on the mixing process by imposing either fully developed turbulent or laminar flow at the inlets. Turbulent boundary conditions were generated by simulating the flow separately in a square duct with periodic boundary conditions in the streamwise direction. As shown in S3 of ESI†, our first and second order statistics of the square duct flow agree very well with references values from literature^{34,35}. The simulated data were stored over time at a given cross-section and then prescribed at the inlet during the simulation of the T-mixer. Fig. 3 shows the inlet streamwise velocity v over x at mid height for the laminar velocity profile (red, Re -independent in dimensionless form), the time-averaged and an instantaneous turbulent velocity profile (black) at $Re = 4000$. In addition, a modified laminar flow (blue) preserving the cross-sectional volume flux is shown. This was used to test the sensitivity of the dynamics observed in the intermediate regime to inflow boundary conditions (see §3.2).

2.1.3 Intensity of segregation

All the statistical data presented in the paper were obtained over a time interval of $200d/u_0$ following a transient of $40d/u_0$, over which data is not collected. We quantified the mixing efficiency with the intensity of segregation³⁶

$$I_s = \frac{\sigma_b}{\sigma_{\max}}, \quad (3)$$

which is 1 (0) for completely segregated (perfectly mixed) streams. Here σ_{\max} is the maximum variance (determined by completely segregated streams),

$$\sigma_{\max}^2 = \langle \phi \rangle (1 - \langle \phi \rangle) \quad (4)$$

and σ_b is the mean square deviation of the concentration profile

$$\sigma_b^2 = \frac{1}{S_{\text{tot}}} \int_S (\phi - \langle \phi \rangle)^2 dy dz = \frac{1}{S_{\text{tot}}} \sum_{i=1}^N S_i (\phi_i - \langle \phi \rangle)^2. \quad (5)$$

The mean concentration is

$$\langle \phi \rangle = \frac{1}{S_{\text{tot}}} \sum_{i=1}^N S_i \phi_i,$$

where S_{tot} (S_i) is the area of the cross section (control volume i) and N the number of control volumes in the cross-section.

2.2 Experimental methods

The main channel of the T-mixer and the inlets were milled into a piece of stainless steel and covered by a plate of the same material that was cold-welded on top. Both inlets were connected to in-house build piston-pumps with a volume of 50 ml each. Both pistons were moved simultaneously in their glass-barrels by a stepping motor with gear reduction enabling a pulsation-free flow. The pressure at each inlet was monitored with a sampling rate of 1 kHz using pressure transmitters (model A09 from Sensor-Technik Wiedemann GmbH, Germany). A LabView2009 program was developed to control the pistons and to monitor the pressure. In order to be able to scan different Reynolds numbers within one experimental run, a program was developed to realize several consecutive flow rates without interruption. The temperature of the barrels was kept at $20 \pm 1^\circ\text{C}$ using a LAUDA Alpha R8 cooling thermostat.

Pressure loss measurements are the first essential step in a comparative study between simulation and experiment. In our numerical simulations, pressure losses were measured from the inlets to the outlet. In the experiments, pressure probes were installed before the connectors to the inlets of the T-mixer to avoid disturbances to the fluid flow. As a result, the experimental measurements included also the losses due the connector and the additional 15mm of inlet. Their contribution was measured independently in a separate set of experiments, in which the T-mixer was replaced by a square duct of 15mm in length. This was subtracted from the total loss measured in the mixing experiments, thereby allowing a direct comparison to the simulations (see Fig. S4 in ESI† for a sketch). Finally, we note that at low Reynolds numbers ($Re \lesssim 400$) the pressure loss was of the order of the measurement uncertainty, hence large errors were expected in this regime.

Chemical reactions, used as molecular probes for mixing, are powerful tools to gain insights into the mixing process. We here used the common Villermoux–Dushman reaction^{10,21} to quantify the mixing efficiency. Details of the employed chemical components, experimental protocols and data analysis are in S5 of ESI†.

3 Mixing regimes

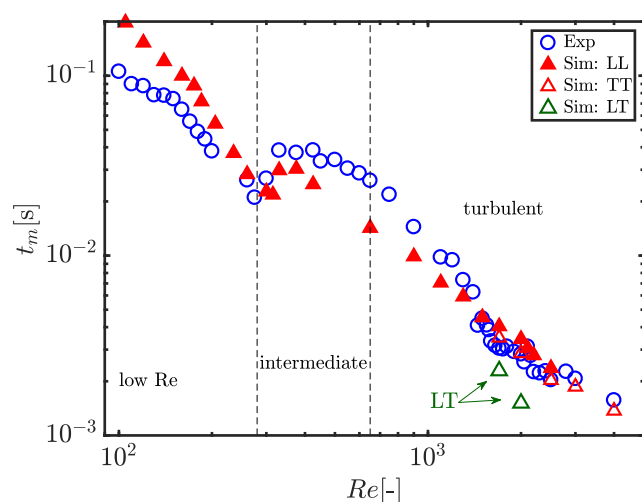


Fig. 4 Experimentally measured mixing time t_m (circles) and computationally estimated mixing time using Eq. 6 (triangles) as a function of Re . Three mixing regimes are highlighted: *low Re*, *intermediate* and *turbulent*. These are separately discussed in §3.1, §3.2 and §3.3, respectively. \blacktriangle and \triangle triangles represent laminar-laminar (LL) and turbulent-turbulent (TT) inflow conditions, respectively. Data with laminar-turbulent (LT) inflow conditions are indicated with an arrow. The influence of the different inflow conditions is discussed in §3.3.

The mixing efficiency is quantified in the Villermux–Dushman characterization^{10,21} with the mixing time t_m (or normalized segregation index X_s), which is the time needed to achieve the final segregation between two competitive reaction products in relation to the initial feed concentration. By contrast, the mixing efficiency is quantified in the simulations with the dimensionless intensity of segregation I_s (eq. 3), which measures the *local* segregation at a particular point in the mixing device (here the outlet). In order to allow a comparison between simulation and experiment, the intensity of segregation is multiplied here by the mean residence time from the junction to the outlet $t_r = 12d/u_0$. We find that the simple empirical relationship

$$t_m = 1.8 I_s \cdot t_r, \quad (6)$$

renders excellent agreement between the numerically and experimentally determined mixing time, especially in the high Re -regime ($Re \gtrsim 1500$). The empirical factor 1.8 was chosen here such that the experimental t_m and the numerical $I_s \cdot t_r$ match exactly at $Re = 2500$. This particular Reynolds number was selected to avoid the hydrodynamic complexities of the transitional regime ($Re < 2000$) and to ensure that fully developed flow was present in the inlet channels of the T-mixer. We note that in the Villermux–Dushman characterization the conversion from the segregation index X_s to mixing time is accomplished through an empirical constant as well (see Fig. S5 in ESI†). The qualitative changes observed in the mixing efficiency as Re increases are elucidated in what follows.

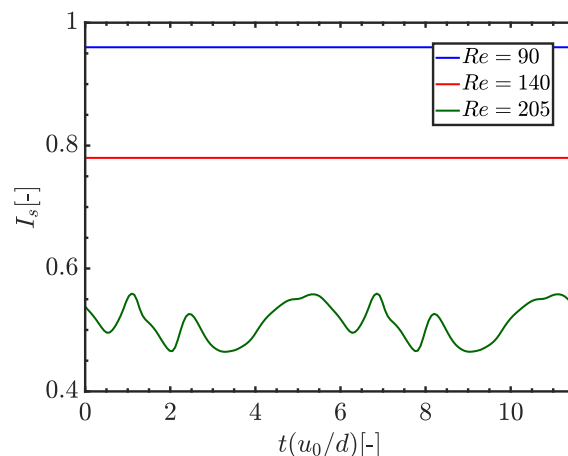


Fig. 5 Temporal evolution of the segregation index I_s at $x = 11.5$ for various Reynolds numbers.

3.1 Low Reynolds number regime

When the Reynolds number is arbitrarily small (Stokes flow), the flow has no vortices (*stratified* regime), and the inlet streams collide and flow side by side along the mixing channel. As Re increases, four symmetric vortices gradually arise at the junction, but the planar interface persists, as shown generically by the colormap of ϕ in Fig. 1(c). Because the flow is left-right symmetric in both the stratified and the vortex regimes, mixing occurs only via molecular diffusion at the planar interface, whose width grows approximately as $\sqrt{2Dx/u_0}$ ³⁷. In our simulations, this vortex regime was found stable up to $Re_c \approx 105$, at which point it was superseded by two counter-rotating vortices which break the reflection symmetry. They engulf and rotate the inlet streams along the main channel, resulting in an increase of mixing efficiency due to the enlarged interface area, see Fig. 1(d). The *engulfment* regime is a robust feature of T-mixers, but its onset depends slightly on the height-to-width aspect ratio of both inlet and outlet channels¹⁴. As Re was further increased, the flow began to pulsate periodically in time as shown in Fig. 5. This marked the transition from the steady to the time-periodic engulfment regime, which was observed at $Re \approx 175$ in the simulations and at $Re \approx 160$ in the experiments. The two engulfing vortices remain, but the locations of their cores pulsate periodically with time. This unsteadiness enhances mixing, as seen in the change of slope of t_m in Fig. 4.

The experimentally measured mixing time t_m is lower than that estimated numerically. This can be explained as follows. At low Re , the outlet channel was too short for the chemical reaction to complete, see e.g. the segregated streams leaving the outlet channel in Fig. 1(d). We thus suspect that here mixing was enhanced as the fluids steadily dropped in the beaker, and that the fluids continued to mix in the beaker, before being measured off-line in a UV spectrometer (see S5 of ESI†). For example, for $Re < 80$ no experimental measurements were conducted because in the steady vortex regime the mixing time was always determined by the ongoing mixing in the beaker. As Re was increased, the fluids mixed more intensively in the main channel and the ongoing

mixing in the beaker became (relatively) less important. Hence, progressively better agreement between simulation and experiment was achieved by increasing Re .

3.2 Intermediate regime

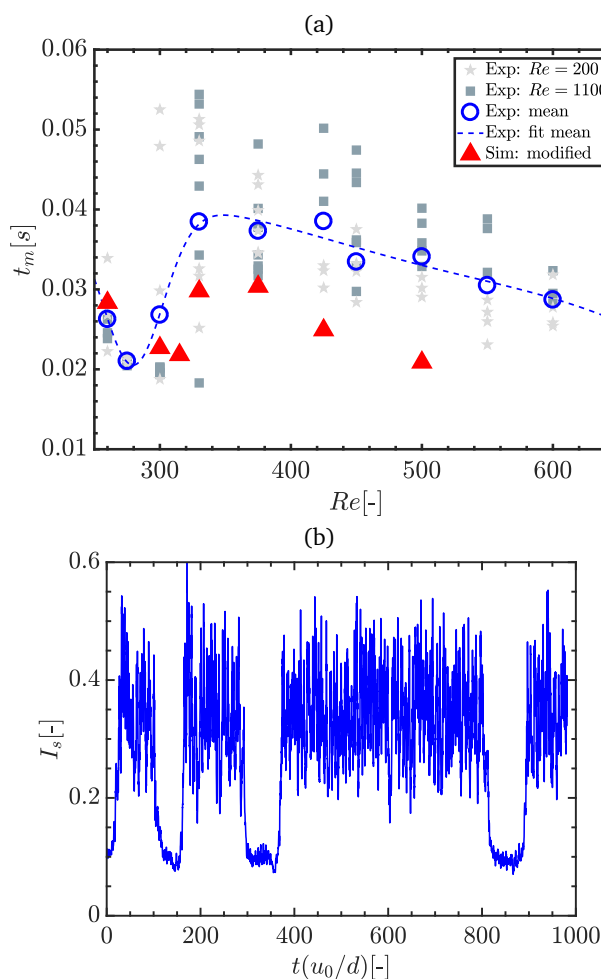


Fig. 6 (a) Experimentally measured mixing time t_m (blank circles) and computationally estimated mixing time using Eq. 6 (triangles) as function of Reynolds number Re . Square and diamond symbols represent t_m of experimental run using initial conditions at $Re = 200$ and $Re = 1100$, respectively. (b) Time history of I_s evaluated shortly after the junction at $x = 2.5$ for $Re = 330$. In the DNS, the modified laminar inflow condition of Fig. 3 was used.

As the Reynolds number is further increased, the engulfment regime is replaced by a four vortex state in which the time-averaged flow field is reflection symmetric. This transition exhibits hysteresis in the simulations and for example at $Re = 330$ the two states (engulfment and symmetric) can be obtained depending on how the system is initialized¹⁸. In the hysteresis region, we attempted to obtain both states in the experiments by using the following procedure. First, the system was run at $Re = 200$ or $Re = 1100$, where only the engulfment or the symmetric are stable, respectively. Then the flow rate was rapidly adjusted, without interruption of the fluid flow, to a target Reynolds number (e.g. $Re = 330$), where the two states should be stable according to the simulations. For each Reynolds number investigated in this in-

termediate regime ($260 \lesssim Re \lesssim 600$), this procedure was repeated several times, but no hysteresis could be detected. Instead, a large variability in the measured mixing time t_m was observed depending on the realization. Fig. 6(a) shows that when averaging over all realizations, a continuous transition from the engulfment to the symmetric regime is recovered. This suggests that either the slightly different inlet profile (which was not fully developed in the experiment for $Re > 360$) or other experimental imperfections triggered dynamic transitions between the two states, resulting in very different t_m depending on how much time the flow exhibited a symmetric or engulfment pattern in each experimental run.

This hypothesis was verified in the numerical simulations by replacing the laminar inlet boundary condition with a modified velocity profile (see the blue line in Fig. 3). With this modified inlet profile, the flow was observed to jump randomly in time between the two states, as shown in the time series of Fig. 6(b) and the flow snapshots of Fig. 1(e)–(f). Hence, modifying the inlet boundary conditions destroyed the hysteresis regime and the same continuous transition as in the experiments was observed in the simulations. Such phenomenology is well known in fluid dynamics³⁸ and will be disseminated separately in detail.

3.3 Transition to turbulence

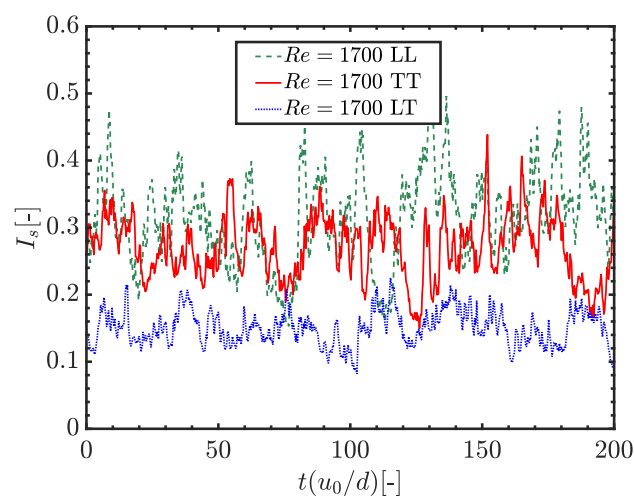


Fig. 7 Temporal evolution of intensity of segregation I_s at $Re = 1700$. Boundary conditions with laminar-laminar (LL), turbulent-turbulent (TT) and laminar-turbulent (LT) inlets are compared. The temporal average of the time series is $\bar{I}_s = 0.32, 0.27$ and 0.18 for LL, TT and LT, respectively.

At $Re \gtrsim 650$ the hysteresis region vanished and only the symmetric state remained regardless of the boundary conditions. To be more precise, the time-averaged velocity field flow is left-right symmetric, but the flow is turbulent, and vortices of different sizes enlarge the fluid interface locally (macromixing), thereby enhancing mixing by molecular diffusion (micromixing). As Re was increased, the turbulent fluctuations raised in the collision zone and the Kolmogorov scale η diminished progressively.

The error bars in Fig. 1(b) show that for $Re \lesssim 1400$ and $Re \gtrsim 2000$ there was little scatter in the experimentally measured t_m , whereas in between large deviations were observed. The perfect

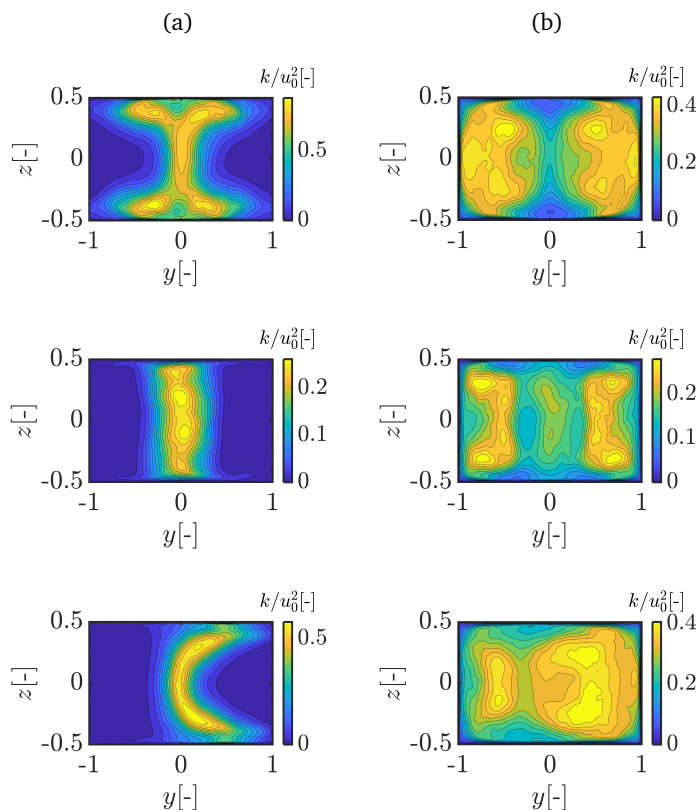


Fig. 8 Colormaps of normalized turbulent kinetic energy k/u_0^2 at two cross-sections, $x = 0.25$ (a) and $x = 1.5$ (b), along the mixing channel at $Re = 1700$. From top to bottom laminar inflows (LL case), turbulent inflows and mixed inflows, consisting of turbulent and laminar inflow from the left side ($y < 0$) and the right side ($y > 0$), respectively, are shown.

overlap of the transitional regime in square-duct flow with the regime in which large scatter was observed in our experiments, strongly suggested that imperfections at the entrance of the lateral ducts triggered turbulent puffs, which then proceeded toward the junction of the T-mixer. We tested this hypothesis both in simulations and experiments.

In the numerical simulations, the flow at the inlet can be prescribed as turbulent or laminar, as explained in §2.1. Although in our experiments there could be a random occurrence of turbulent puffs separated by laminar segments at $Re \in [1400, 2000]$, the details of this process are setup-specific and very expensive to simulate³¹. For simplicity, we simulated three different scenarios at $Re = 1700$: laminar flow at both inlets (LL), turbulent flow at both inlets (TT) and a mixed case (LT), with turbulent flow at the left inlet ($y < 0$) inlet and laminar flow at the right inlet ($y > 0$). For the turbulent inlets, fully turbulent square duct was computed at $Re = 4000$ and was downscaled by a factor of $4000/1700 = 2.35$ to generate the inlet boundary conditions for $Re = 1700$. These three distinct inflow conditions can be seen as the limiting cases for the random collision of traveling puffs expected in experiments.

The temporal evolution of the intensity of segregation I_s with these inlet flow conditions is shown in Fig. 7. For laminar inlets (LL), the average intensity of segregation was $\bar{I}_s = 0.32$, whereas

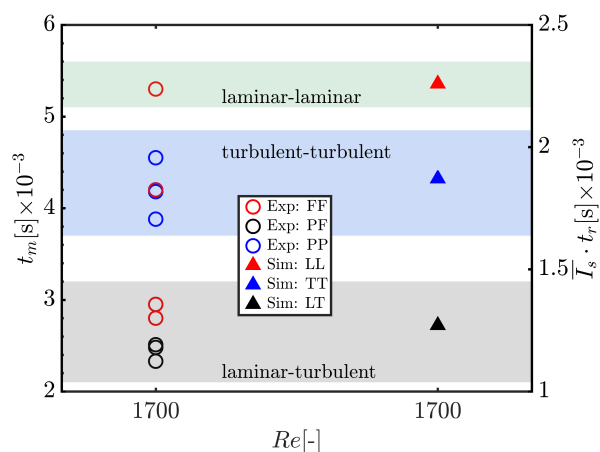


Fig. 9 Experimentally measured mixing time t_m (triangles) and numerically computed intensity of segregation I_s multiplied with the mean residence time t_r (circles) at $Re = 1700$. In both cases, three different inflow conditions were used: free-free (FF), perturbed-free (PF) and perturbed-perturbed (PP) in the experiments, and analogously laminar-laminar (LL), turbulent-turbulent (TT) and laminar-turbulent (LT) in the simulations.

for turbulent inflows (TT) the mixing was better ($\bar{I}_s = 0.27$). Surprisingly, the mixed case (LT) yielded a vast improvement of the mixing efficiency with $\bar{I}_s = 0.18$. The reason for this behavior stems from the shape of the collision interface at the junction of the T-mixer, which initiates and determines the development of the mixing process along the outlet channel. Fig. 8 shows snapshots of the turbulent kinetic energy k at $x = 0.25$ (top row) and $x = 1.5$ (bottom row) in the mixing channel for the three inflow cases considered. For laminar inflows, the influence of the parabolic shape of the laminar inflow profile is seen in the collision interface, which yields the highest turbulent intensities at the top and bottom walls and a thin layer of quiescent intensities at the peak of the parabola, see Fig. 8(a). By contrast, for the turbulent inflows a broad interface with the highest intensities in the center was found, see Fig. 8(b). For the mixed inflow conditions, a biased parabolic shape with the highest intensities was found, but in contrast to LL case, the highest intensities are distributed along the parabola and not at the walls. This left-right asymmetry of the velocity field persists along the mixing channel (see the bottom row of Fig. 8) and accounts for the better mixing. While in the LL and TT cases the mixing is driven only by the fluctuations due to turbulent vortices, in the LT case the mean flow pattern also contributes to the mixing of the inlet streams, in an analogous manner to the asymmetric flow pattern of the engulfment regime. Note that in all cases the Reynolds number was identical at the two inlets, so the mass flow rate of the colliding streams was identical, and the impingement point remained in average at the center.

In order to avoid the random generation of turbulent puffs in the experiments, we introduced helices made of wire in the cone of the inflow pipe (entrance to the square duct). This produced a turbulent inflow as used in the simulations. Three distinct inlet conditions were tested at $Re = 1700$ (free-free: FF, perturbed-free:

PF, perturbed-perturbed: PP). When the disturbance was applied at both inlets (PP), the micro-mixing time was $t_m \approx 4.3 \times 10^{-3}$ s and exhibited a small standard deviation (2×10^{-4} s). When only one of the two inflows was disturbed (PF), mixing was greatly enhanced with $t_m \approx 2.4 \times 10^{-3}$ s. We performed four experimental runs with two undisturbed inlets (FF), and observed a great variation depending on the experimental realization. In two cases, the same t_m as PP was observed, in one instance as in PF, and in another instance, much poorer mixing was observed, exactly as expected from the collision of two laminar inflows. The comparison of the experimentally measured t_m with the numerically computed I_s is shown in Fig. 9 and confirms the influence of the inflow condition on the quality of mixing.

3.4 Fully turbulent regime

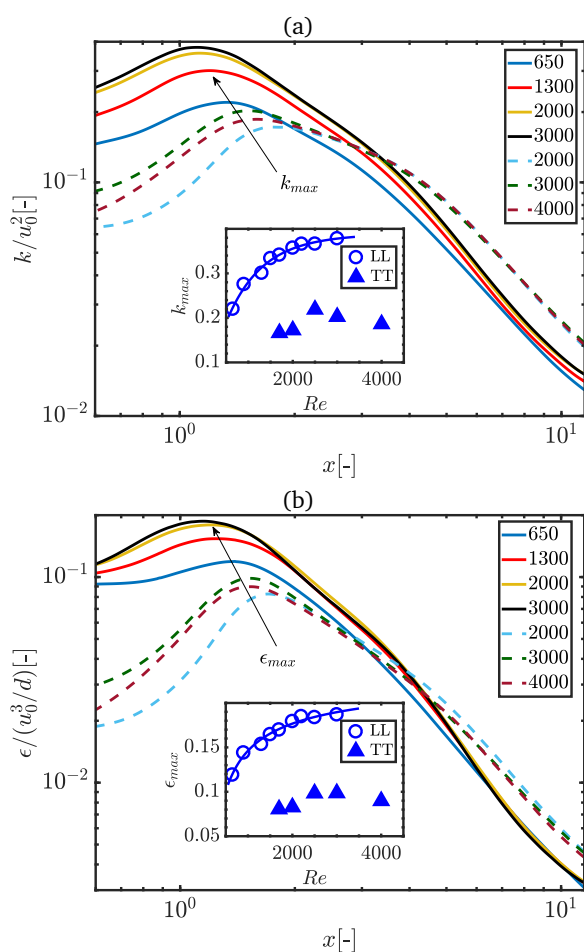


Fig. 10 (a) Normalized turbulent kinetic energy k/u_0^2 and dissipation (b) $\epsilon/(u_0^3/d)$ along the mixing channel for various Reynolds numbers with laminar (solid line) and turbulent (dashed line) inflow conditions. The inset shows the maximum value k_{\max} and ϵ_{\max} of k/u_0^2 and $\epsilon/(u_0^3/d)$, respectively, as function of Re .

As the Reynolds number was increased beyond $Re > 2000$, the mixing time t_m continued to improve, but much more slowly as shown in Fig. 4. While such an asymptotic behavior of t_m was observed experimentally in several mixers^{9,39–43}, it remains poorly

understood. Our simulations resolve all temporal and spatial scales in turbulence, allowing a more detailed analysis than possible in past studies. Figs. 10 shows the evolution of the normalized turbulent kinetic energy k/u_0^2 and dissipation $\epsilon/(u_0^3/d)$, both averaged over the cross-section, along the mixing channel axis for several Re in the turbulent regime. Initially, both quantities increase as turbulence intensifies due to the collision of the two incoming streams, and subsequently, a maximum is reached before turbulent fluctuations (and thus dissipation) begin to decay. This onset of decay also marks the onset of strong mixing, and the decay behavior is fairly independent of the Reynolds number Re and is mainly determined by the inflow conditions (LL/TT). The insets of Figs. 10 show that for each inflow condition, the maximum values of the normalized turbulent kinetic energy and dissipation increase, but finally saturate as Re increases. This is in agreement with the asymptotic theoretical scalings $k \propto Re^2$ and $\epsilon \propto Re^3$ for isotropic turbulence. As turbulence in the T-mixer reaches the asymptotically behavior, the improvement of the mixing efficiency also approaches an asymptotic state and results in a slow decrease of t_m , as observed for $Re \gtrsim 2000$.

Note also that the LL case exhibits larger dissipation than TT, which may be surprising in view that turbulent inlets dissipate more than laminar ones. However, laminar inflow profiles are quasi-parabolic and thus carry much more kinetic energy than flat turbulent inflow profiles (see Fig. 3). This excess energy results in larger dissipation in the main (mixing) channel. As the dissipation at the inlets is negligible compared to the dissipation in the mixing channel, laminar inlets cause a larger net dissipation.

4 Specific power input and mixing time

Mixing models such as the interplay of exchange with the mean (IEM)²¹, the engulfment diffusion deformation (EDD)⁷ or the incorporation⁴⁴ micromixing model, are widely used to predict and characterize mixing and reaction outcomes. They especially find application at high Schmidt number flows to quantify micromixing. Their common underlying assumption is that within the lifetime of a small eddy $t_\eta = (\nu/\epsilon)^{0.5}$ micromixing is completed, thus assuming implicitly that the turbulent dissipation determines mixing. In practice, the turbulent dissipation is typically estimated as $\epsilon_{\Delta p} = \Delta p Q / (\rho V)$, where Δp is the pressure loss, Q is the volume flow rate, and V is the volume of fluid in the T-mixer. The micromixing time is then estimated in the aforementioned models as $t_m \propto t_\eta \simeq (\nu/\epsilon_{\Delta p})^{0.5}$, see Falk and Commenge¹⁰.

Fig. 11(a) shows that in our T-mixer $\epsilon_{\Delta p}$ is nearly independent of the inlet boundary conditions, whereas the mixing time is mainly determined by them. In fact, at the same Re laminar inlets feature slightly higher dissipation than turbulent inlets, whereas the mixing time is lower for the latter. Remarkably, by using a laminar and a turbulent inlet at $Re = 2000$ in the simulations, the same mixing time as $Re = 4000$ with two turbulent inlets could be achieved. Given that the pressure loss is not much affected by the inlet conditions, this implies that the energy dissipation is about six times lower, as shown in Fig. 11(a). In other words, the same mixing time can be achieved at $Re = 2000$, but with a specific power input of only ≈ 600 W/kg instead of the ≈ 3500 W/kg needed to operate at $Re = 4000$. Unfortunately, in our experiments

we could only keep the inlets laminar up to $Re = 1700$. By disturbing one inlet and keeping the other laminar, we could achieve the same mixing time as for $Re = 2200$ with turbulent inlets. The energy dissipation was $\varepsilon_{\Delta p} = 560\text{W/kg}$ and 1200W/kg , respectively, i.e. a factor of 2 lower. This demonstrates that the dissipated energy or input power can be a poor estimator of mixing, in contrast to the commonly accepted view and the underlying assumption of the aforementioned models, i.e. $t_m \propto (\nu/\varepsilon_{\Delta p})^{0.5}$. While our experimental and numerical data exhibit this scaling in the fully turbulent regime, the boundary conditions have a significant impact.

Finally, we stress that the dependence of the mixing time on the energy dissipation shown in Fig. 11(b) is close to that obtained by Falk and Commenge¹⁰ using a variety of mixers (see their Fig. 5). Our study covers the whole range of their mixing times, but for the same dissipation, our mixing times are roughly three times lower in average than theirs. For the specific case of mixed laminar-turbulent inflow conditions at $Re = 2000$, our mixing time is even six times lower than theirs.

5 Conclusion

Turbulence models based on the Reynolds-averaged Navier–Stokes equations (RANS) or simple empirical micromixing models are typically used to design chemical reactors. Their accuracy, and more importantly, their transferability to new situations is however doubtful. Because of the increase in computing power in the last decades years, DNS of fluid flows at operationally relevant regimes are now possible. They allow accurate predictions of turbulent mixing and comparisons to laboratory experiments, as done here for a simple T-shaped mixer. The highest attained $Re = 4000$ is well beyond previous experimental and numerical works, which have mostly focused on moderate Reynolds numbers, e.g. up to $Re = 400$ ¹⁹ in a T-mixer and $Re = 1100$ in Confined Impinging Jet Reactor^{45,46}.

A detailed macroscopic description of mixing as presented here is key to predict the qualitative outcome of mixing-sensitive chemical reactions or precipitation processes in the liquid phase. The good agreement between the numerically computed segregation index I_s and experimentally measured mixing time t_m support the validity of our approach. This suggests a predominant role of turbulent eddies (or macromixing) in controlling the mixing efficiency. However, caution must be taken because of the freedom in the factor used to compare the two data sets, i.e. here $t_m = 1.8I_s \cdot t_r$. Changing this factor allows an arbitrary vertical shift between the two data sets in Fig. 4. Despite this fact, the agreement in the trends (and slopes of the curves) indicates that either our numerical scheme models micromixing in a reasonable fashion, or that micromixing can be easily parametrized if macromixing is well resolved in the simulations. This result is very encouraging and suggests that by solving for chemical reactions simultaneously with the Navier–Stokes equations should lead to a quantitative prediction of mixing-sensitive reactions.

Finally, our experimental and numerical findings reveal the importance of inlet boundary conditions in determining the efficiency of mixing. More specifically, we could show that by using mixed laminar-turbulent inflow conditions a six-fold reduction of the specific power input could be reached at constant mix-

ing time. Future work will include experiments with longer inlet channels and precisely controlled inflow conditions to test the limits of this technique. For example, in continuous chemical synthesis, fast mixing is key for mixing-sensitive reactions. However, because of the exponential raise in the viscosity of the solvent with temperature (operating with external cooling), the increase of the pressure drop, thus the inflow rate, is limited in practice¹. Manipulating the boundary conditions might be a promising and simple method to enhance mixing at low Reynolds numbers as well.

Conflicts of interest

There are no conflicts to declare.

Acknowledgements

The authors would like to acknowledge the funding of the Deutsche Forschungsgemeinschaft (DFG) through the Cluster of Excellence Engineering of Advanced Materials (EAM) and Bayer Technology Services GmbH (BTS). The authors gratefully acknowledge the compute resources and support provided by the Erlangen Regional Computing Center (RRZE).

References

- 1 H. Kim, K.-I. Min, K. Inoue, D.-P. Kim, J.-i. Yoshida *et al.*, *Science*, 2016, **352**, 691–694.
- 2 K. F. Jensen, *AIChE Journal*, 2017, **63**, 858–869.
- 3 M. B. Plutschack, B. Pieber, K. Gilmore and P. H. Seeberger, *Chemical reviews*, 2017, **117**, 11796–11893.
- 4 H.-C. Schwarzer and W. Peukert, *Chemical engineering & technology*, 2002, **25**, 657–661.
- 5 B. K. Johnson and R. K. Prud'homme, *Phys. Rev. Lett.*, 2003, **91**, 118302.
- 6 R. Karnik, F. Gu, P. Basto, C. Cannizzaro, L. Dean, W. Kyei-Manu, R. Langer and O. C. Farokhzad, *Nano letters*, 2008, **8**, 2906–2912.
- 7 J. Bałdyga and J. R. Bourne, *Turbulent mixing and chemical reactions*, Wiley, 1999.
- 8 H. Bockhorn, D. Mewes, W. Peukert and H. Wernecke, *Micro and Macro Mixing*, Springer, 2010.
- 9 H. Nagasawa, N. Aoki and K. Mae, *Chemical engineering & technology*, 2005, **28**, 324–330.
- 10 L. Falk and J.-M. Commenge, *Chemical Engineering Science*, 2010, **65**, 405–411.
- 11 A. Fani, S. Camarri and M. V. Salvetti, *Physics of Fluids*, 2013, **25**, 064102.
- 12 M. Hoffmann, M. Schlüter and N. Rübiger, *Chemical engineering science*, 2006, **61**, 2968–2976.
- 13 D. Bothe, C. Stemich and H.-J. Warnecke, *Chemical Engineering Science*, 2006, **61**, 2950–2958.
- 14 R. Poole, M. Alfateh and A. Gauntlett, *Chemical Engineering Science*, 2013, **104**, 839–848.
- 15 A. Soleymani, E. Kolehmainen and I. Turunen, *Chemical engineering journal*, 2008, **135**, S219–S228.
- 16 S. Thomas and T. A. Ameel, *Experiments in fluids*, 2010, **49**, 1231–1245.

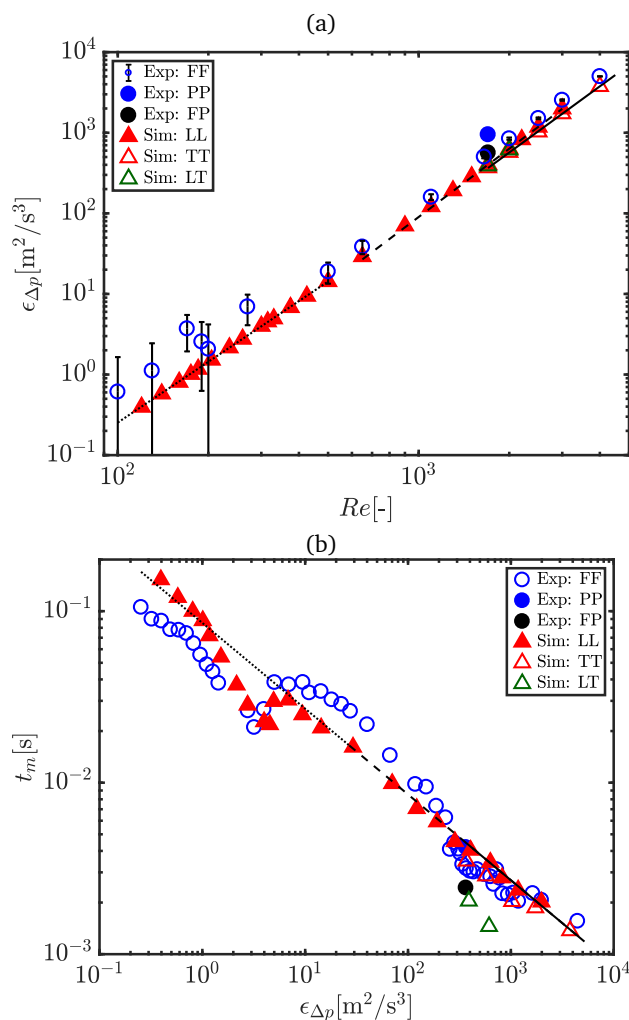


Fig. 11 (a) Turbulent dissipation $\epsilon_{\Delta p}$ estimated from the pressure loss Δp as function of Reynolds number Re comparing experiments and simulations while considering all three inflow scenarios: free-free (FF), perturbed-free (PF) and perturbed-perturbed (PP) in the experiments, and analogously laminar-laminar (LL), turbulent-turbulent (TT) and laminar-turbulent (LT) in the simulations. (b) Experimentally measured mixing time t_m and computationally estimated mixing time using Eq. 6 as a function of energy dissipation $\epsilon_{\Delta p}$ in $Re = (90, 4000)$. In case of t_m , $\epsilon_{\Delta p}$ is estimated from the power law fit obtained in (a). Straight lines show the theoretical relation $t_m = (\nu/\epsilon_{\Delta p})^{0.5}$.

17 A. Fani, S. Camarri and M. V. Salvetti, *Physics of Fluids*, 2014, **26**, 074101.
 18 T. Schikarski, W. Peukert and M. Avila, *Chemical Engineering Journal*, 2017, **324**, 168–181.
 19 A. Mariotti, C. Galletti, R. Mauri, M. V. Salvetti and E. Brunazzi, *Chemical Engineering Journal*, 2018, **341**, 414–431.
 20 P. Moin and K. Mahesh, *Annual review of fluid mechanics*,

1998, **30**, 539–578.

21 J.-M. Commenge and L. Falk, *Chemical Engineering and Processing: Process Intensification*, 2011, **50**, 979–990.
 22 G. Beavers, E. M. Sparrow and R. Magnuson, *International Journal of Heat and Mass Transfer*, 1970, **13**, 689–701.
 23 Y. A. Cengel and J. M. Cimbala, *Fluid Mechanics: Fundamentals and Applications - Third Edition*, McGraw-Hill Higher Education, Boston, 2006.
 24 M.-C. Fournier, L. Falk and J. Villiermaux, *Chemical Engineering Science*, 1996, **51**, 5053–5064.
 25 N. P. Waterson and H. Deconinck, *Journal of Computational Physics*, 2007, **224**, 182–207.
 26 J. Jeong and F. Hussain, *J. Fluid. Mech*, 1995, **285**, 69–94.
 27 A. de Lozar and B. Hof, *arXiv preprint arXiv:1001.2481*, 2010.
 28 K. Takeishi, G. Kawahara, H. Wakabayashi, M. Uhlmann and A. Pinelli, *J. Fluid. Mech*, 2015, **782**, 368–379.
 29 O. Reynolds, *Phil. Trans. R. Soc. Lond.*, 1883, **174**, 935–982.
 30 I. J. Wygnanski and F. H. Champagne, *J. Fluid Mech.*, 1973, **59**, 281–335.
 31 M. Avila and B. Hof, *Phys. Rev. E*, 2013, **87**, 063012.
 32 D. Barkley, B. Song, V. Mukund, G. Lemoult, M. Avila and B. Hof, *Nature*, 2015, **526**, 550–553.
 33 D. Barkley, *J. Fluid. Mech*, 2016, **803**, P1.
 34 A. Pinelli, M. Uhlmann, A. Sekimoto and G. Kawahara, *J. Fluid. Mech*, 2010, **644**, 107–122.
 35 S. Gavrilakis, *J. Fluid. Mech*, 1992, **244**, 101–129.
 36 P. Danckwerts, *Applied Scientific Research, Section A*, 1952, **3**, 279–296.
 37 P. Tabeling, *Introduction to microfluidics*, Oxford University Press on Demand, 2005.
 38 D. S. Zimmerman, S. A. Triana and D. P. Lathrop, *Physics of Fluids*, 2011, **23**, 065104.
 39 N. Aoki and K. Mae, *Chemical Engineering Journal*, 2006, **118**, 189–197.
 40 M. Kashid, A. Renken and L. Kiwi-Minsker, *Chemical engineering journal*, 2011, **167**, 436–443.
 41 L. Zhendong, L. Yangcheng, W. Jiawei and L. Guangsheng, *Chemical Engineering Journal*, 2012, **181**, 597–606.
 42 N. Kockmann, T. Kiefer, M. Engler and P. Woias, *Sensors and Actuators B: Chemical*, 2006, **117**, 495–508.
 43 S. W. Siddiqui, Y. Zhao, A. Kukukova and S. M. Kresta, *Industrial & Engineering Chemistry Research*, 2009, **48**, 7945–7958.
 44 J. Villiermaux and L. Falk, *Chemical Engineering Science*, 1994, **49**, 5127–5140.
 45 J. Gradl and W. Peukert, *Chemical Engineering Science*, 2009, **64**, 709–720.
 46 F. Schwertfirm, J. Gradl, H. C. Schwarzer, W. Peukert and M. Manhart, *International Journal of Heat and Fluid Flow*, 2007, **28**, 1429–1442.

Supplementary information

Inflow boundary conditions determine T-mixer efficiency

Tobias Schikarski,^a Holger Trzenschiok,^a Wolfgang Peukert,^a and Marc Avila^b

^a *Institute of Particle Technology, Department of Chemical and Biological Engineering, Friedrich-Alexander-Universität Erlangen-Nürnberg, 91058 Erlangen, Germany; E-mail: tobias.schikarski@fau.de*

^b *Center of Applied Space Technology and Microgravity, Universität Bremen, Am Fallturm, 28359 Bremen, Germany*

Contents

S1 Transition to turbulence	1
S2 The intensity of turbulence in a T-mixer	2
S3 Turbulent statistics of square duct flow	3
S4 Pressure drop measurements	5
S5 Villermaux-Dushman Reaction	6
S5.1 Background	7
S5.2 Notes on mixing time	7
S5.3 Experimental protocols	8

S1 Transition to turbulence

In section §3, we argue that the natural and random occurrence of turbulent puffs beyond $Re \gtrsim 1460$ influences mixing in the outlet channel and results in a large deviation in mixing time t_m (see Fig. 1b in paper). To support this statement, the standard deviation of mixing time, normalized by the mean $\text{std}(t_m)/t_m$, is

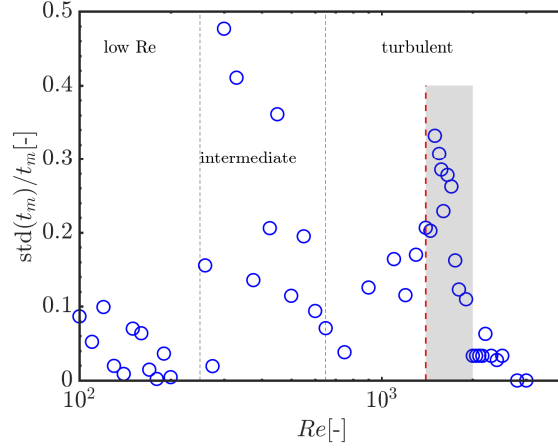


Fig. S1: Standard deviation of the experimentally obtained mixing time, scaled with the mean $\text{std}(t_m)/t_m$, as function of Reynolds number Re . The gray-shaded area depicts the Reynolds number range where turbulent puffs are expected to occur, whereas the red dashed line marks the natural onset of transition, which in our experiments is at $Re \approx 1400$.

shown as a function of Reynolds number in Fig. S1. Clearly, the deviation in measured mixing time increases strongly in the regime where turbulent puffs can occur. Besides, large deviations are also observed in the intermediate regime, where engulfing and symmetric flow structures compete. This emphasizes the general sensitivity of mixing on the inflow in the T-mixer.

S2 The intensity of turbulence in a T-mixer

The collision of inlet streams is used in common mixing devices to trigger strong turbulent motions, hence mixing, at relatively low inflow Reynolds numbers. The accurate computation of the turbulent statistics in our simulation method allows to estimate the turbulent intensity in the mixing channel and compare it to canonical flows, e.g. pipe flow. To do so, the definition of the Taylor microscale for homogeneous isotropic turbulence, $\lambda = \sqrt{10\nu k/\epsilon}$, where k and ϵ are the turbulent kinetic energy and the dissipation, respectively, is assumed to hold. Then, the turbulent Reynolds number $Re_\lambda = \sqrt{k}\lambda/\nu$ can be calculated by extracting the values of k and ϵ from Figure 10. Taking the maximum values of k and ϵ (at around $x = (1, 2)$), we obtain $Re_\lambda \approx 50$ and $Re_\lambda \approx 125$ for $Re = 650$ and $Re = 4000$, respectively. Comparing these values to pipe flow (S.C.C. Bailey *et al.*¹ we are not aware of any study in square duct flow providing similar data), the turbulence level in a T-mixer at $Re = 4000$ is comparable to $Re \approx 60000$ in cylindrical pipe flow.

A more direct comparison to square-duct flow can be done by comparing the pressure loss Δp of our

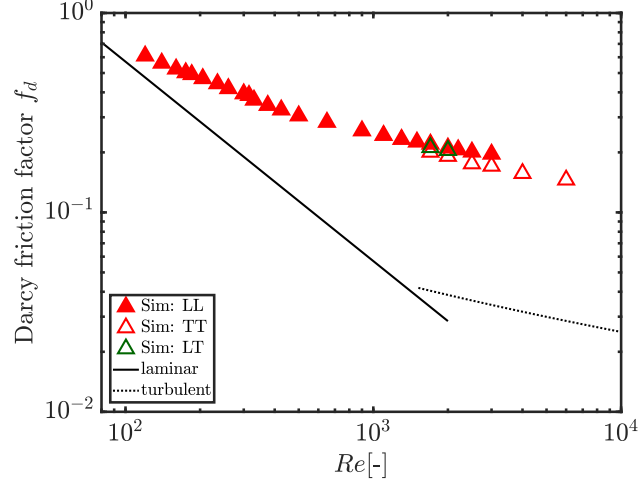


Fig. S2: Darcy friction factor, as defined in Eq. (3), as function of Reynolds number Re . Symbols represent the data obtained from simulation in the T-mixer. The solid and the dashed line denote the laminar and turbulent friction factor of square duct-flow, see Eqs. (4) and (5) respectively.

T-mixer to that of a square duct of the same length by using the Darcy friction factor

$$f_d = 2 \frac{\Delta p d_h}{L \rho u_0^2}, \quad (3)$$

where d_h is hydraulic diameter (of the outlet in case of the T-mixer), u_0 is the mean velocity and L , here $15.5d$, is the length between inlet and outlet. In square duct flow, the Darcy friction factor is

$$f_d = \frac{57}{Re}, \quad (4)$$

for fully developed laminar flow, whereas in the fully turbulent regime it is commonly estimated with an empirical correlation proposed by Jones⁹

$$f_d^{-1/2} = 2 \log_{10}(2.25 Re f_d^{1/2}) - 0.8. \quad (5)$$

Fig. S2 shows that at low Re the friction factor of the T-mixer is close the laminar value of square-duct flow. However, as Re increases, the friction factor gradually departs from it because of the subsequent hydrodynamic instabilities, which result in turbulent flow at the junction. As the turbulence develops fully, the friction factor of the T-mixer appears to evolve nearly parallel to that of square-duct flow, but it is about 5 times larger in magnitude.

S3 Turbulent statistics of square duct flow

In our simulations of the flow in a T-mixer at large Re , we apply fully developed turbulent flow at the inlet boundaries. To generate a fully developed turbulent inflow, we simulated the fluid flow at the desired

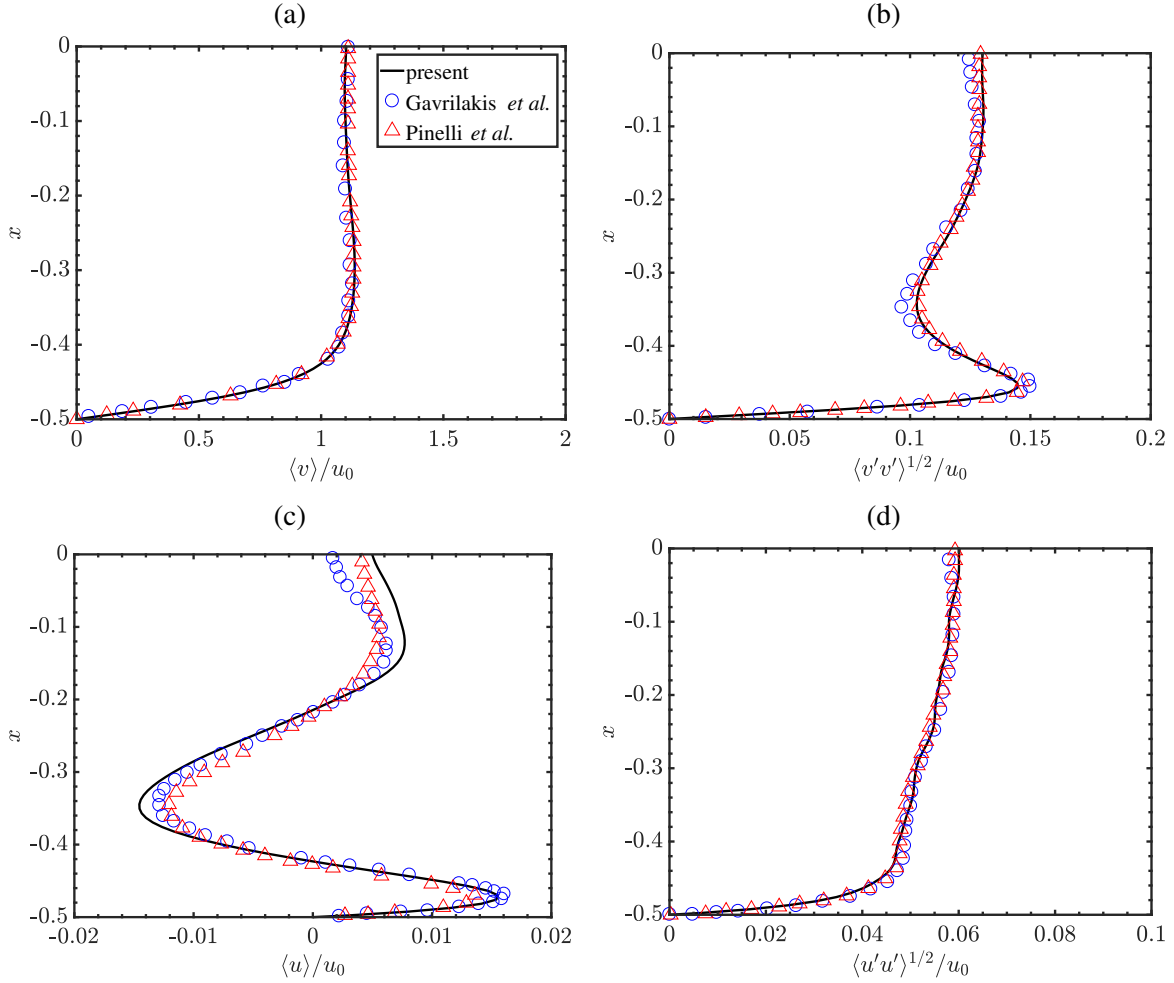


Fig. S3: Turbulent statistics (black line) obtained at $Re = 4000$ are compared to reference data (blue circles¹² and red triangles⁶) obtained at $Re = 4410$. (a) and (b) show the mean $\langle(\bullet)\rangle$ and root mean square velocity $\langle(\bullet)'(\bullet)'\rangle^{1/2}$ components at position $z = 0.35$, respectively. The top and bottom row depict the streamwise v and cross-stream u velocity component, respectively. Note that the orientation of coordinates of the T-mixer inlet are used as well as only the half of the channel width is shown.

Reynolds number in a periodic square duct with stream-wise length of $L = 30d$ (see Fig. 6 in paper) and mapped the stored data for two selected cross sections to the two inlet boundaries of the T-mixer. To avoid correlated results, the data of the two cross sections is used with $100d/u_0$ delay.

Fig. S3 shows a comparison of the first and second order turbulent statistics obtained with the our DNS to reference data^{6,12} at a fixed height, here $z = 0.35$. We averaged our data in time and in the (homogeneous) streamwise direction, which is denoted by the operator $\langle \rangle$. Good agreement between our simulations and the reference simulations in the mean velocity components $\langle u \rangle$ and $\langle v \rangle$ (see Fig. S3(a)) was obtained. Slight deviations apart from the wall in cross-stream velocity component $\langle v \rangle$ are attributed to the too short average time interval. Similar, the normal Reynolds stresses $\langle u'u' \rangle^{1/2}$ and $\langle v'v' \rangle^{1/2}$, where $u' = u - \langle u \rangle$ describes the velocity fluctuations, agree very well to the reference data (see Fig.S3(b)).

S4 Pressure drop measurements

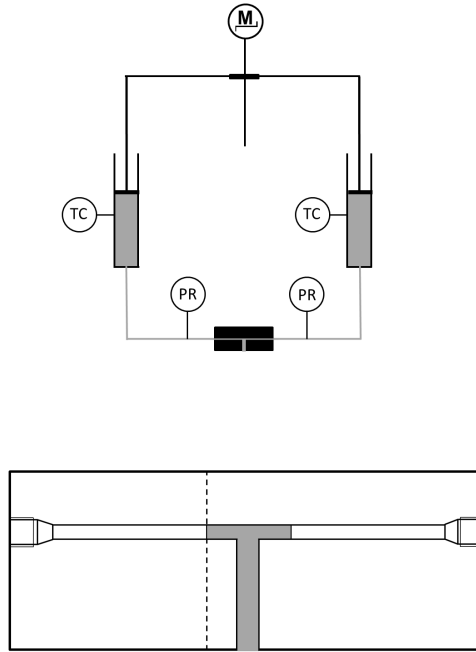


Fig. S4: (a) Sketch of the experimental setup. (M), (TC) and (PR) denote the stepping motor, temperature-controlled barrels and the position of the pressure recording, respectively. A zoom of the T-mixer is shown in (b). The grey shaded T-mixer depicts the domain used in the simulations.

Fig. S4 shows a sketch of the full experimental setup, which consists of two inlets of square cross section of hydraulic diameter $d = 1\text{mm}$, which discharge in a mixing channel of 1mm height, 2mm width and

11.5mm length. The inlets are 18mm long, whereas in the simulations the inlets are just 3mm long because we impose fully developed flow as boundary condition. The geometry of the simulations is shown gray shaded in Fig. S4. Pressure transmitters model A09 (Sensor-Technik Wiedemann GmbH, Germany) with a range up to 0.5bar relative pressure were used to measure the pressure difference between the fluid in the T-mixer and the environment. To avoid disturbing the inflow close to the junction, we did not install pressure probes at the locations of the simulated geometry (i.e. 3mm before the junction). Instead, the pressure probes were installed before the connections to the inlets of the T-mixer device (PR). To enable comparison with the simulations, a second device consisting of a square duct of 15mm length was manufactured (the dashed line in Fig. S4(b) depicts the position its outlet). With this second device, experiments were performed to measure the pressure loss. This was then subtracted from the total loss measured in the experiments with the actual T-mixer, thereby allowing a direct comparison to the simulations.

Before each experimental run, a baseline pressure signal was recorded for 5 seconds. Then, after the pistons started moving and the flow structures developed, the pressure signal reached a plateau, indicating operation in steady-state conditions. For each experiment, the average pressure of the baseline was subtracted to the average steady-state pressure. Finally, we note that at low Reynolds numbers (up to Re 400) the resulting pressure loss is of the order of the measurement uncertainty. Although deviations are expected, the agreement with numerical simulations is excellent, see Fig. 11(a) in § 4 (paper).

S5 Villermaux-Dushman Reaction

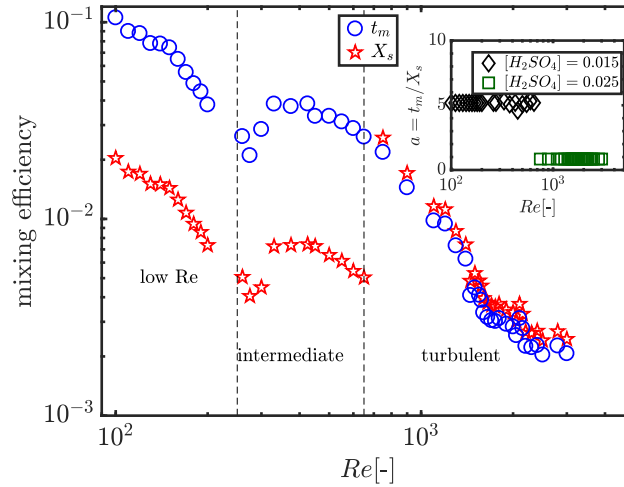


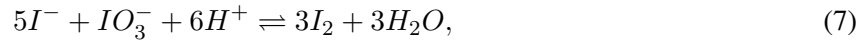
Fig. S5: Experimentally obtained mixing efficiencies (segregation index X_s [-] and mixing time t_m [s]) as function of the Reynolds number. The inset shows the concentration dependence of $a = t_m/X_s$ as function of Reynolds number Re .

S5.1 Background

Chemical reactions, used as molecular probes for mixing, are powerful tools to gain insights into the mixing process. In the literature, several competitive consecutive and parallel chemical reactions have been proposed, where the distribution of quantifiable chemical species depicts the mixing history.^{10,11,13} Fournier *et al.*⁵ proposed the parallel use of the neutralization of boric acid



with the Dushman–reaction³



namely the Villiermaux–Dushman reaction,² to quantify the mixing efficiency of mixing devices. In this reaction system, sulfuric acid is added in a stoichiometric deficit. If mixing is nearly perfect, then sulfuric acid is entirely consumed due to the very fast kinetics, whereas if mixing is poor the by-product iodine I_2 emerges from the Dushman reaction.

While the neutralization of boric acid in Eq. 6 is quasi-instantaneous, the kinetics of the Dushman reaction is much slower and in the range of the mixing process.⁸ The iodine formed in the redox-reaction will further react in a quasi-instantaneous reaction with iodide ions and form an equilibrium with triiodide-ions,⁷ which reads



The concentration of the formed triiodide ions I_3^- was measured here with a Cary 100 Scan UV/Vis spectrometer (Varian Deutschland GmbH) at a wavelength of 353 nm and quantified by applying the Beer–Lambert law

$$[I_3^-] = \frac{OD}{\epsilon_{353} \cdot l} \quad \text{valid if } 0.1 < OD < 2.5, \quad (9)$$

where OD, ϵ_{353} and l denote the optical density (absorbance), the extinction coefficient of triiodide at wavelength 353nm and the optical path length within the measurement cell, respectively. Note that the UV/VIS spectrometer was not connected to the mixing setup. Thus the samples collected in a beaker were measured offline. In doing so, at least 1.5ml of the mixture was collected for each experimental trial, while 1ml of this collected amount was needed for optical density measurements itself.

S5.2 Notes on mixing time

The mixing efficiency is quantified in the Villiermaux–Dushman characterization by the segregation index

$$X_s = \frac{Y}{Y_{st}}, \quad (10)$$

which is the fraction of H^+ ions used to form iodine I_2 , i.e.

$$Y = \frac{[I_2] + [I_3^-]}{[H^+]_0} \quad \text{and} \quad Y_{st} = \frac{6[IO_3^-]_0}{[IO_3^-]_0 + [H_2BO_3^-]_0}, \quad (11)$$

where the subscript $_0$ denotes the initial concentration. The weakness of this approach lies in the dependence of the segregation index X_s on the initial concentrations. In our experiments, the mixing efficiency changes enormously as Re increases from 100 to 4000, and this requires the application of different concentrations sets to stay in the linear regime of the detector of the spectrometer (see Eq. 9). However, using different concentrations sets results in a discontinuous transition in the segregation index X_s as the Reynolds number increases, see Fig. S5. Two different concentrations sets are applied in this study (see Tab. S1), which are changed at $Re = 650$.

Commenge *et al.*² solved this problem by providing a single empirical a master curve capturing multiple concentration sets. In particular, their master curve converts the measured optical density (effectively the segregation index) into a mixing time

$$t_m = 0.33(OD)[H^+]_0^{-4.55}[I^-]_0^{-1.5}[IO_3^-]_0^{-5.8}[NaOH]_0^{-2}[H_3BO_3]_0^{-2}. \quad (12)$$

Their approach relies on the interaction of exchange with the mean (IEM) model, which incorporates the influence of the mixing time t_m on the Villermux-Dushman reaction and the actual reaction system including the kinetics.^{2,4} By varying the mixing time in the model, different segregation indices X_s were obtained and compared to the measured ones. Doing this for different mixers, Reynolds numbers and concentration sets, large datasets were gathered and collapsed together on one master curve by normalizing with the product of reactant concentrations as introduced above in Eq. 12. Two of the concentration sets given in their work enabled the seamless identification of mixing times between 0.1 and 0.001s in our work, whereby the actual concentrations are given in Tab. S1.

In practice, within one concentration set the mixing time t_m can be obtained by just multiplying a constant factor to the segregation index X_s as

$$t_m \approx a \cdot X_s, \quad (13)$$

where the constant a depends solely on the concentration set as depicted in Fig. S5. Thus, the herein used mixing time t_m is nothing else than a normalized segregation index.

S5.3 Experimental protocols

Impurities brought into the reaction system can drastically change the kinetics of chemical reactions. This could occur either by unwanted alternative reactions or by merely changing the ionic strength. To detect such problems, our T-mixer was carefully cleaned every day before and after the experimental runs. Each experiment was repeated at least three times and at different days using solutions freshly prepared each day.

Tab. S1: Base concentrations and acid concentrations used for the Villiermaux–Dushman reaction.

Reactants		concentrations mol l ⁻¹	
		$Re = (100, 650)$	$Re = (700, 4000)$
acid	H ₂ SO ₄	0.015	0.025
base	NaI		0.032
	KIO ₃		0.006
	NaOH		0.09
	H ₃ BO ₃		0.09

In all experiments, ultrapure water, produced with a Purelab[®] Ultra from Elga LabWater (Veolia Water Solutions & Technologies, France), was used. For the Villiermaux–Dushman characterization, the chemicals used were all of high purity, either analytical grade (p.a. or Reag. PhEur) or of 99.8% purity. Sulfuric acid 96% (p.a.), potassium iodate (p.a.) (Carl Roth GmbH, Germany), sodium iodite (Reag. Ph Eur) (Merk KGaA, Germany), sodium hydroxide (reagent grade)(Sigma-Aldrich Chemie GmbH, Germany) and boric acid (99,8%) (Alfa Aesar, Germany) were used. The solutions were prepared as described by Guichardon *et al.*⁷ to prevent thermodynamic triiodide formation. Additionally, before the solutions were prepared, the ultrapure water was stripped with nitrogen gas to avoid the oxidation of iodide to iodine.⁸ The employed chemicals do not influence the material parameter of the aqueous solution, e.g. viscosity and density, and thus enable to compare the results qualitatively between simulation and experiment.

Additional References

- ¹ Sean CC Bailey, Marcus Hultmark, Joerg Schumacher, Victor Yakhot, and Alexander J Smits. Measurement of local dissipation scales in turbulent pipe flow. *Physical review letters*, 103(1):014502, 2009.
- ² Jean-Marc Commenge and Laurent Falk. Villiermaux–dushman protocol for experimental characterization of micromixers. *Chemical Engineering and Processing: Process Intensification*, 50(10):979–990, 2011.
- ³ Saul Dushman. The rate of the reaction between iodic and hydriodic acids. *The Journal of Physical Chemistry*, 8(7):453–482, 1904.
- ⁴ L Falk and J-M Commenge. Performance comparison of micromixers. *Chemical Engineering Science*, 65(1):405–411, 2010.
- ⁵ M-C Fournier, L Falk, and J Villiermaux. A new parallel competing reaction system for assessing micromixing efficiencyexperimental approach. *Chemical Engineering Science*, 51(22):5053–5064, 1996.
- ⁶ S Gavrilakis. Numerical simulation of low-reynolds-number turbulent flow through a straight square duct. *J. Fluid. Mech.*, 244:101–129, 1992.

- ⁷ Pierrette Guichardon and Laurent Falk. Characterisation of micromixing efficiency by the iodide–iodate reaction system. part i: experimental procedure. *Chemical Engineering Science*, 55(19):4233–4243, 2000.
- ⁸ Pierrette Guichardon, Laurent Falk, and Jacques Villiermaux. Characterisation of micromixing efficiency by the iodide–iodate reaction system. part ii: kinetic study. *Chemical Engineering Science*, 55(19):4245–4253, 2000.
- ⁹ OC Jones. An improvement in the calculation of turbulent friction in rectangular ducts. *Journal of Fluids Engineering*, 98(2):173–180, 1976.
- ¹⁰ Felix Nabholz and Paul Rys. Chemical selectivities disguised by mass diffusion. iv. mixing-disguised nitrations of aromatic compounds with nitronium salts. 4th communication on the selectivity of chemical processes. *Helvetica Chimica Acta*, 60(8):2937–2943, 1977.
- ¹¹ Edward L Paul and Robert E Treybal. Mixing and product distribution for a liquid-phase, second-order, competitive-consecutive reaction. *AIChE Journal*, 17(3):718–724, 1971.
- ¹² Alfredo Pinelli, Markus Uhlmann, Atsushi Sekimoto, and Genta Kawahara. Reynolds number dependence of mean flow structure in square duct turbulence. *J. Fluid. Mech*, 644:107–122, 2010.
- ¹³ Shengyao Yu. *Micromixing and parallel reactions*. PhD thesis, ETH Zurich, 1993.